Switchable axionic magnetoelectric effect via spin-flop transition in topological antiferromagnets

Yiliang Fan,[1,*] Rongxiang Zhu,[1,*] Tongshuai Zhu,[2] Jianzhou Zhao,[3] Huaiqiang Wang,[4,5,†] and Haijun Zhang[1,5,6,7,8,‡]

[1]*National Laboratory of Solid State Microstructures, School of Physics, Nanjing University, Nanjing 210093, China*
[2]*College of Science, China University of Petroleum (East China), Qingdao 266580, China*
[3]*Department of Physics, School of Science, Tianjin University, Tianjin 300354, China*
[4]*Center for Quantum Transport and Thermal Energy Science, Institute of Physics Frontiers and Interdisciplinary Sciences, School of Physics and Technology, Nanjing Normal University, Nanjing 210023, China*
[5]*Jiangsu Physical Science Research Center, Nanjing 210093, China*
[6]*Collaborative Innovation Center of Advanced Microstructures, Nanjing University, Nanjing 210093, China*
[7]*Jiangsu Key Laboratory of Quantum Information Science and Technology, Nanjing University, Suzhou 215163, China*
[8]*Shishan Laboratory, Suzhou Campus of Nanjing University, Suzhou 215000, China*

(Received 20 November 2025; revised 20 March 2026; accepted 21 April 2026; published 19 May 2026)

The $MnBi_2Te_4$ material family has emerged as a key platform for exploring magnetic topological phases, most notably exemplified by the experimental realization of the axion insulator state. The interplay between spin dynamics and axion states in topological magnets is anticipated to lead to rich phenomena that yet remain largely unexplored. In this work, we employ an antiferromagnetic spin-chain model to demonstrate that an external magnetic field induces perpendicular magnetic anisotropy. We find that an in-plane field stabilizes the antiferromagnetic order, whereas an out-of-plane field destabilizes it and triggers spin-flop transitions. Remarkably, near the surface spin-flop transition in even-layer $MnBi_2Te_4$ films, the axion insulator state undergoes a sharp switching behavior accompanied by distinct magnetoelectric responses. Furthermore, we propose that this switchable axionic magnetoelectric effect can be utilized to convert alternating magnetic field signals into measurable square-wave magneto-optical outputs, thereby realizing an axionic analog of a zero-crossing detector.

DOI: 10.1103/cmpk-d882

I. INTRODUCTION

In topological field theory, the electromagnetic response of three-dimensional insulators is described by an axion action $S_\theta = (\theta/2\pi)(\alpha/2\pi)\int d^3x\, dt\, \mathbf{E}\cdot\mathbf{B}$ [1,2], where $\alpha = e^2/\hbar c$ is the fine-structure constant, $\mathbf{E}$ and $\mathbf{B}$ are the electric and magnetic fields, respectively, and θ is a dimensionless pseudoscalar field known as the axion field [3]. When the insulator preserves either time-reversal or spatial-inversion symmetry, θ becomes quantized to either 0 or π (mod 2π), corresponding to topologically trivial and nontrivial phases, respectively. The quantized θ gives rise to a range of interesting phenomena, such as the topological magnetoelectric effect [4–6], quantized magneto-optical Faraday/Kerr rotation [7,8], and half-quantized Hall conductance [9–11]. Realizing those phenomena requires gapped surface states by breaking the time-reversal symmetry (TRS) on the surface of topological insulators (TIs) [12–16]. The recently discovered layered antiferromagnetic (AFM) TI $MnBi_2Te_4$ [17–24] featuring both a nontrivial $\theta = \pi$ term and gapped surface states, has emerged as a prominent platform for topological magnetoelectric effects. For instance, odd-septuple-layer (SL) $MnBi_2Te_4$ films exhibit the quantum anomalous Hall (QAH) effect [25–29], while even-SL films feature the axion insulator state [16,20,30–32] and quantum-metric-induced nonlinear transport [33,34].

Rich phenomena related to $MnBi_2Te_4$ stem from the interplay between its nontrivial band topology and distinctive *A*-type AFM order [35,36], where each SL features out-of-plane ferromagnetic (FM) ordering and adjacent SLs are coupled antiferromagnetically. Interestingly, the AFM spin dynamics in layered $MnBi_2Te_4$ films are expected to give unconventional physical phenomena not observed in traditional magnetic materials [27,37–40]. For example, a cascade of quantum phase transitions induced by spin flips and flops has been discovered in the QAH state of $MnBi_2Te_4$ [27,41]. However, to our knowledge, the influence of AFM spin dynamics on the axion insulator state and the resultant topological magnetoelectric effect in $MnBi_2Te_4$-like layered systems yet remains unexplored.

In this work, based on an AFM spin-chain model for layered antiferromagnets, we demonstrate that an applied magnetic field effectively induces emergent magnetic anisotropy perpendicular to the field direction, as illustrated in Figs. 1(a) and 1(b). Specifically, a magnetic field applied perpendicular to the easy axis enhances the magnetic anisotropy and stabilizes the AFM order, whereas a field parallel to the axis destabilizes the AFM order and further triggers a spin-flop transition. Notably, the spin-flop transition profoundly influences the axion insulator state in $MnBi_2Te_4$ films, thereby triggering a drastic change of the axionic magnetoelectric

*These authors contributed equally to this work.
†Contact author: hqwang@njnu.edu.cn
‡Contact author: zhanghj@nju.edu.cn

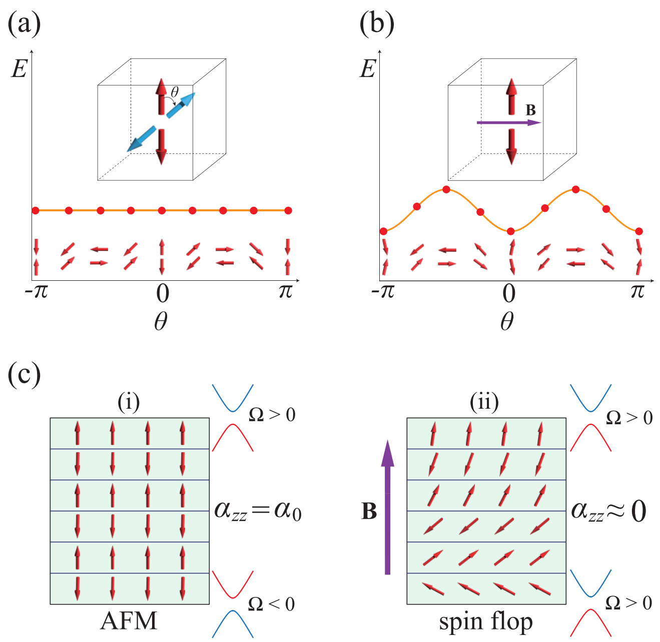

FIG. 1. (a),(b) Schematics of the field-induced perpendicular magnetic anisotropy. (a) In the absence of an external field, the magnetic energy landscape is isotropic with respect to the Néel vector orientation. (b) Under an applied magnetic field, two energy minima emerge where the Néel vector aligns perpendicular to the field direction. (c) Illustration of spin configurations, Berry curvatures of surface states, and out-of-plane magnetoelectric coefficient for even-SL AFM TIs (i) before and (ii) after the spin-flop transition induced by an external field.

response, as shown by distinct surface Berry curvature configurations and out-of-plane magnetoelectric coefficients in Fig. 1(c). Furthermore, we propose that near the spin-flop transition point, a weak out-of-plane AC magnetic field can periodically switch the axionic magnetoelectric response each time the field passes through zero. This conversion of the sinusoidal input field into a square-wave axionic response output can be experimentally read out via magneto-optical spectroscopy, thereby realizing an axionic analog of a zero-crossing detector common in signal processing.

II. COMPUTATIONAL METHODS

The first-principles calculations are carried out using the Perdew-Burke-Ernzerhof-type generalized gradient approximation (GGA) [42] of the density functional theory, using the Vienna *Ab initio* Simulation Package (VASP) [43]. The calculations incorporate spin-orbit coupling, and the GGA + U approach with $U = 5.0$ eV is adopted to account for the correlated effects in $MnBi_2Te_4$. A plane-wave energy cutoff of 400 eV is employed.

For the bulk $MnBi_2Te_4$, the interlayer magnetic exchange constant is quantified by calculating the magnetic energy difference between FM and A-type AFM configurations. The magnetic anisotropy constant is determined from the energy difference between in-plane and out-of-plane magnetic orders. The same approach is employed to calculate the magnetic anisotropy constant for the monolayer system.

III. FIELD-INDUCED PERPENDICULAR MAGNETIC ANISOTROPY AND SPIN-FLOP TRANSITION

We model the magnetic structure of even-SL $MnBi_2Te_4$ film exhibiting the axion insulator state as a one-dimensional AFM spin chain with $2N$ sites, representing each FM SL by an effective spin ($\mathbf{S}_i$) that is antiferromagnetically coupled to its nearest neighbors along the out-of-plane (z) direction. Under an external magnetic field $\mathbf{B}$, the spin-chain Hamiltonian can be described by

$$H = -g\mu_B \sum_{i=1}^{2N} \mathbf{B}\cdot\mathbf{S}_i + J\sum_{i=1}^{2N-1} \mathbf{S}_i\cdot\mathbf{S}_{i+1} - D_z\sum_{i=1}^{2N}\left(S_i^z\right)^2. \quad (1)$$

Here, the first term represents the conventional linear Zeeman coupling between each spin and magnetic field, with g and μ_B denoting the Landé g factor and Bohr magneton, respectively. The second term describes the AFM exchange coupling ($J > 0$) between neighboring SLs. The third term accounts for the intrinsic uniaxial magnetocrystalline anisotropy along the out-of-plane direction, characterized by the anisotropy constant D_z. The competition among these energy terms leads to a variety of intriguing magnetic phases and rich spin dynamics, most notably the spin-flop transition.

In the thermodynamic limit ($N \to \infty$), the system admits a macrospin description. Under this approximation, the sublattice magnetizations are represented by two macroscopic spins, $\mathbf{M}_{A,B} = g\mu_B \sum_{i\in A,B}\mathbf{S}_i$, which can be parametrized as $\mathbf{M}_{A,B} \approx M(\sin\theta_{A,B}\hat{x} + \cos\theta_{A,B}\hat{z})$, with $M = g\mu_B NS$. To track the orientation of the Néel vector under an external field, we introduce two collective variables. The tilting angle $\theta = (\theta_A + \theta_B - \pi)/2$ defines the orientation of the Néel vector relative to the z axis, while $\theta_c = (\theta_A - \theta_B)/2$ characterizes the canting angle between the two sublattice spins. Then the average magnetic energy $E(\theta, \theta_c)$ can be derived (see Appendix A for details). Following the principle of energy minimization, the effective energy $E(\theta)$ as a function of the tilting angle θ is obtained by minimizing the total energy $E(\theta, \theta_c)$ with respect to the canting angle θ_c.

We begin by considering a simplified case containing only the isotropic AFM exchange coupling and the linear Zeeman term, with the magnetic field applied along the x direction. The solid energy curves $E(\theta)$ in Fig. 2(a) show that the Zeeman term breaks the isotropy of the AFM structure. This symmetry breaking generates a pair of degenerate minima at $\theta = 0$ and π, corresponding to the Néel vector aligning along the $+z$ and $-z$ directions, respectively. Thus, the applied magnetic field establishes an extrinsic magnetic anisotropy, thereby pinning the easy axis perpendicular to itself. This conclusion is further confirmed by the field dependence of the Néel vector component L_z shown in Fig. 2(b). Upon applying an infinitesimal B_x, L_z immediately jumps to a finite value of $2\mu_B$, signaling the abrupt alignment of the Néel vector along the easy axis. Despite the increasing spin canting along the x direction with B_x, the Néel vector remains robustly pinned along the z axis.

We now proceed to incorporate the out-of-plane uniaxial magnetic anisotropy term inherent to layered $MnBi_2Te_4$ films and investigate two representative configurations with in-plane (B_x) and out-of-plane (B_z) magnetic fields,

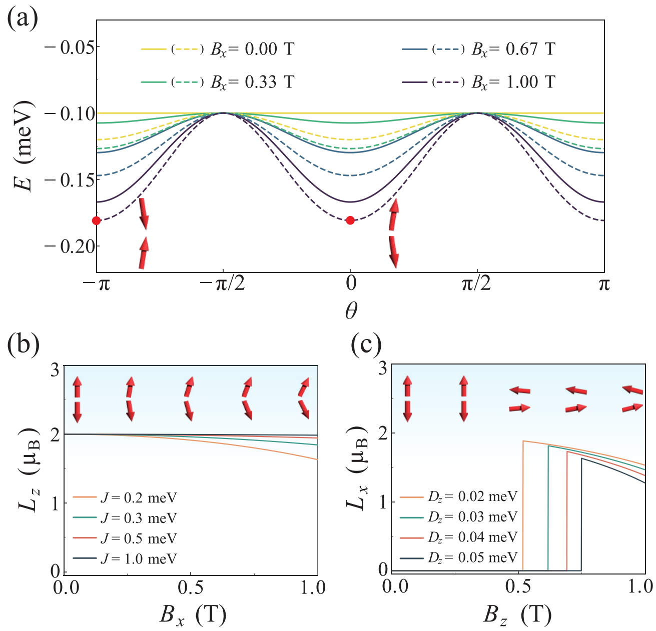

FIG. 2. (a) Magnetic anisotropy energy vs Néel vector orientation under in-plane magnetic fields (B_x), considering only the linear Zeeman coupling: without the uniaxial anisotropy (solid lines) and with out-of-plane anisotropy (dashed lines, $D_z = 0.02$ meV). (b) Out-of-plane component (L_z) of the Néel vector as a function of in-plane field (B_x) for different interlayer exchange couplings (J). Insets: Schematics of spin configurations under different B_x with $J = 0.2$ meV. (c) In-plane component (L_x) of the Néel vector as a function of out-of-plane field B_z for different out-of-plane anisotropy constants. Insets: Schematics of spin configurations under different B_z with $D_z = 0.02$ meV. In the calculations above, we assume that each spin carries an angular momentum of 1/2 $\hbar$.

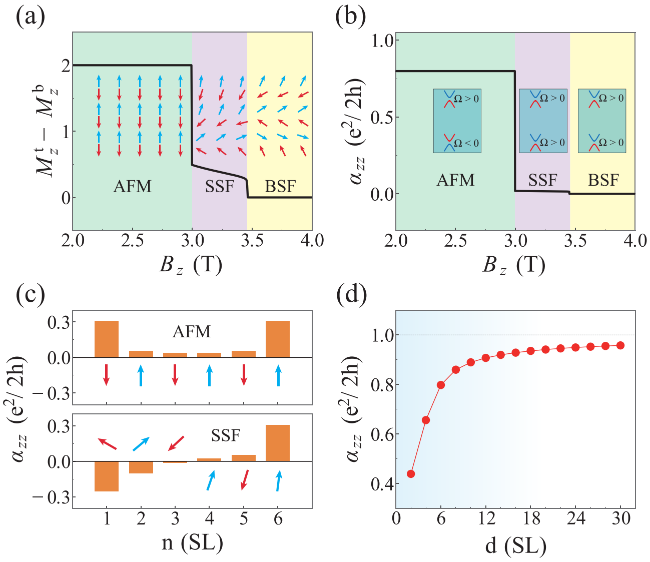

FIG. 3. (a) Evolution of spin configurations in each SL and the difference between the z components of the normalized magnetic moments for the top and bottom surfaces vs out-of-plane magnetic field B_z in a six-SL $MnBi_2Te_4$ film, obtained from atomistic spin simulations. Surface spin-flop (SSF) and bulk spin-flop (BSF) transitions occur at $B_z = 3.00$ and 3.45 T, respectively. (b) The out-of-plane magnetoelectric coupling coefficient α_{zz} and corresponding surface Berry curvature configurations as a function of out-of-plane magnetic field B_z. (c) Layer-resolved magnetoelectric coupling coefficient α_{zz} in the AFM state (upper panel) and the SSF (lower panel) state. (d) Thickness dependence of α_{zz}, illustrating the finite-size effect. The parameters of the atomistic spin simulations are $J = 1.01$ meV (AFM exchange constant), $D_z = 0.23$ meV (uniaxial anisotropy constant), and $M_s = 5\mu_B$ (magnetic moment). The parameters of the Dirac-fermion model are $v_F = 5 \times 10^5$ m/s, $\Delta_S = 84$ meV, $\Delta_D = -127$ meV, $J_S = 36$ meV, and $J_D = 29$ meV.

respectively. Under an in-plane field B_x, the Zeeman term reinforces the perpendicular orientation of the Néel vector, thereby cooperating with the intrinsic uniaxial anisotropy to strengthen the out-of-plane easy axis, as evidenced by the dashed lines in Fig. 2(a). In contrast, an out-of-plane field B_z favors an in-plane Néel vector, which competes with the intrinsic out-of-plane anisotropy. Consequently, upon increasing B_z to a critical value, the system undergoes an AFM spin-flop transition, characterized by an abrupt reorientation of the Néel vector from out-of-plane to in-plane directions [Fig. 2(c)]. Furthermore, we have performed atomistic spin simulations based on the Landau-Lifshitz-Gilbert equation (see Appendix G), which are in good agreement with our theoretical analysis.

IV. AXIONIC MAGNETOELECTRIC RESPONSE ACROSS THE SPIN-FLOP TRANSITION

Given that the axion field in even-SL $MnBi_2Te_4$ films depends on the magnetic configurations [30,44,45], the AFM spin-flop transition involving a drastic reconfiguration of spins is therefore expected to profoundly influence the axionic magnetoelectric response. Owing to the experimental availability of high-quality samples and advanced magnetoelectric measurement capabilities [32], we select the six-SL $MnBi_2Te_4$ film as a representative system for our study. We model the spin-flop transition in a six-SL $MnBi_2Te_4$ film using atomistic spin simulations of a six-spin chain under out-of-plane magnetic fields, with input parameters obtained directly from first-principles calculations (see Appendix D for details). Our simulations reveal two spin-flop transitions at critical fields of 3.00 and 3.45 T [see Fig. 3(a)], corresponding to the surface spin-flop (SSF) and bulk spin-flop (BSF) transitions, respectively. Before the SSF transition, the system retains the A-type AFM order. Upon the SSF transition, the system exhibits an asymmetrically canted AFM order. Specifically, the spins near the top surface remain close to the out-of-plane direction, while those at the bottom surface tilt significantly toward the in-plane direction, as evidenced by the difference in the z components of their magnetic moments in Fig. 3(a). This behavior originates from the interplay between the modified exchange couplings and magnetocrystalline anisotropy near the surface [37,39]. Beyond the BSF transition, the top and bottom surface spins cant at an identical angle, which is smaller than the uniform canting angle exhibited by bulk spins.

To investigate the axionic magnetoelectric response of $MnBi_2Te_4$ films, we employ the Dirac-fermion approach for layered magnetic TIs, where each SL is effectively modeled by two Dirac-cone states located on its top and bottom surfaces, respectively. Within this framework, an N-SL $MnBi_2Te_4$ can be described by the following Hamiltonian [46,47]:

$$H = \sum_{\mathbf{k}} \sum_{i,j=1}^{N} \left[\left(v_F \tau_z (k_x\sigma_y - k_y\sigma_x) + \mathbf{m}_i \cdot \boldsymbol{\sigma} + \Delta_S \tau_x \right) \delta_{i,j} + \Delta_D \tau_- \delta_{j,i+1} + \Delta_D \tau_+ \delta_{j,i-1} \right] c^\dagger_{\mathbf{k}i} c_{\mathbf{k}j}. \tag{2}$$

Here, v_F is the Fermi velocity, σ and τ are Pauli matrices acting in the spin and top-bottom surface subspaces, respectively, with $\tau_\pm = (\tau_x \pm i\tau_y)/2$. The Δ_S and Δ_D terms represent the coupling of top and bottom Dirac surface states within the same SL and between neighboring SLs, respectively. The $\mathbf{m}_i \cdot \boldsymbol{\sigma}$ term describes the Zeeman coupling of the two Dirac surface states of each SL to the effective exchange fields generated by the local magnetic moments. The $\mathbf{m}_i$ of each SL is defined by

$$\mathbf{m}_i = \begin{pmatrix} \mathbf{m}_i^{\mathrm{t}} & 0 \\ 0 & \mathbf{m}_i^{\mathrm{b}} \end{pmatrix}, \tag{3}$$

where $\mathbf{m}_i^{\mathrm{t}}$ and $\mathbf{m}_i^{\mathrm{b}}$ represent the effective exchange fields acting on the top and bottom Dirac surface states, respectively. These fields are determined by the local magnetic moments $\mathbf{m}_i^{\mathrm{t}} = J_S\mathbf{M}_i + J_D\mathbf{M}_{i-1}$ and $\mathbf{m}_i^{\mathrm{b}} = J_S\mathbf{M}_i + J_D\mathbf{M}_{i+1}$. Here, J_S and J_D denote the intra-SL and inter-SL exchange-coupling constants, respectively, while $\mathbf{M}_i$ is the magnetic moment direction of the ith SL. The local magnetic moment directions $\mathbf{M}_i$ are extracted directly from the atomistic spin simulations described above. In our theoretical framework, the spin configuration serves as an external input to the Dirac-fermion model. Consequently, there is no self-consistent feedback from the electronic band structure back to the spin energies, which poses a limitation for exact quantitative predictions. Nevertheless, the model remains robust in capturing the underlying physical mechanisms. The parameters of the model are taken from Ref. [46]: $v_F = 5 \times 10^5$ m/s, $\Delta_S = 84$ meV, $\Delta_D = -127$ meV, $J_S = 36$ meV, and $J_D = 29$ meV.

Based on the above Dirac-fermion model, we calculate the axionic magnetoelectric response using the Kubo formula (see Appendix C for details) [30,48]. Because the axionic magnetoelectric response is isotropic and diagonal, it is sufficient to track the out-of-plane coefficient α_{zz} to characterize this response, as shown in Fig. 3(b). Before the SSF transition, the α_{zz} of the six-SL $MnBi_2Te_4$ film exhibits a nonzero value of approximately $0.8e^2/2h$. Note that the reduction from the quantized value of $e^2/2h$ for an ideal axion insulator originates from the finite-size-induced hybridization between the top and bottom surface states [30,45,49]. This interpretation is confirmed by our thickness-dependent calculation of α_{zz} [Fig. 3(d)], which shows a monotonic increase with film thickness and asymptotically approaches $e^2/2h$ in the thick limit. Upon the SSF transition, the coefficient α_{zz} abruptly drops to nearly zero and falls to zero during the subsequent BSF transition.

The topological magnetoelectric response of six-SL $MnBi_2Te_4$ is governed by its real-space Berry curvature dipole [32], which is defined as the difference between the Berry curvatures of the top and bottom surfaces. For each surface state, the sign of the Berry curvature is determined by its

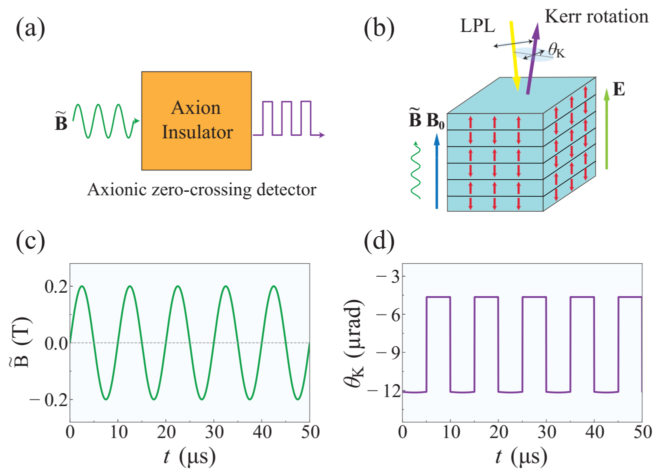

FIG. 4. (a),(b) Schematic of an axionic zero-crossing detector constructed from an even-SL $MnBi_2Te_4$ film, which transforms alternating input magnetic signals to square-wave outputs (a) and experimental setup (b), where a static out-of-plane magnetic field is applied to position the $MnBi_2Te_4$ film at its SSF transition point, and an alternating out-of-plane magnetic field is further applied as the input signal. The output signal is obtained from the magneto-optical Kerr rotation angle measured under normally incident linearly polarized terahertz light in the presence of an out-of-plane electric field. (c),(d) The time-varying input alternating magnetic field (c) and the obtained square-wave-like output (d) from the corresponding Kerr angles under 48.4-THz light.

TRS-breaking Dirac mass, which depends only on the out-of-plane (z) component of the local magnetization. Therefore, even though the SSF state features a canted spin configuration rather than a full spin flip, the reversal of the z component of the bottom surface magnetization is sufficient to invert its Dirac mass. This mass inversion flips the sign of the corresponding Berry curvature, regardless of the in-plane spin canting. Consequently, the topological contributions from the two surfaces largely cancel, quenching α_{zz}. Since only the bottom surface mass is inverted during the SSF transition, the axionic magnetoelectric response is driven toward zero rather than reversing its overall sign. A sign reversal would require mass inversions on both the top and the bottom surfaces. This microscopic mechanism is consistent with the distinct layer-resolved contributions to α_{zz} in the AFM and SSF states, as shown in the upper and lower panels of Fig. 3(c).

V. AXIONIC ZERO-CROSSING DETECTOR

The switchable sharp change in the precedent axionic magnetoelectric coefficient α_{zz} at the SSF transition renders it highly sensitive to small deviations of the external magnetic field from the critical SSF transition field. This unique property can be harnessed to realize an axionic zero-crossing detector, as illustrated in Fig. 4(a), which transforms continuous magnetic field signals to square waves. A zero-crossing detector is an electronic circuit whose core functionality is to detect when an input signal passes through zero potential (the “zero-crossing point”) and produce an instantaneous switch in the output signal at that precise moment. We design the axionic zero-crossing detector as follows. An out-of-plane static magnetic field is applied to position the six-SL $MnBi_2Te_4$ film near its SSF transition point, while a target alternating field is applied along the same direction to serve as the input signal [Fig. 4(b)]. The time-varying target magnetic field drives rapid switching of α_{zz} between its two discrete values, which could be measured by magneto-optical responses acting as square-wave output signals.

For a realistic estimate, the static critical SSF field and the alternating target field are set to $B_0 = 3.0$ T and $\tilde{B} = 0.2\sin(2\pi\nu t)$ T, respectively, with $\nu = 100$ kHz [50]. For the magneto-optical readout, we apply a static out-of-plane electric field E_z ($\epsilon_r E_z = 0.5$ V/nm, where ϵ_r is the relative permittivity) [32] and measure the Kerr rotation angle of normally incident linearly polarized terahertz light. In this normal-incidence geometry, the measured Kerr rotation is determined by the out-of-plane diagonal magnetoelectric coupling coefficient α_{zz}, rendering the proposed axionic zero-crossing detector insensitive to the off-diagonal components that might emerge across the SSF transition [51]. The Kerr rotation angles for different photon energies and magnetic configurations are calculated within the Dirac-fermion framework (see Appendix F). The electric field is incorporated as a layer-resolved potential term in the Dirac-fermion model, which is determined self-consistently by solving the discretized Poisson equation with parameters obtained directly from first-principles calculations of six-SL $MnBi_2Te_4$ (see Appendix E for details). Figure 4(d) presents the resulting time-varying Kerr rotation angle under 48.4-THz (~0.2 eV) light, which transforms the sinusoidal input field [Fig. 4(c)] into square-wave magneto-optical outputs, thus realizing the zero-crossing detection functionality. The predicted Kerr angles are experimentally accessible ($-12 \sim -4.5$ μrad), as demonstrated in recent measurements on $MnBi_2Te_4$ films [32]. Furthermore, because the axionic zero-crossing detector depends on the topological surface states of $MnBi_2Te_4$, its functionality is robust against disorder and defects, as long as these perturbations do not destroy the surface states. The device operation relies on the SSF transition and is consequently limited to temperatures below the Néel temperature of $MnBi_2Te_4$ ($T_N \approx 24.2$ K) [17].

VI. SUMMARY

We present a comprehensive study of the field-tunable axion electrodynamics in $MnBi_2Te_4$ films. Using the spin-chain model for layered antiferromagnets, we reveal that a magnetic field induces emergent perpendicular magnetic anisotropy, which can either stabilize the AFM order or trigger a spin-flop transition. This spin-flop transition profoundly modifies the axion insulator state and switches its magnetoelectric response. We leverage this sharp switching to propose and demonstrate the principle of an axionic zero-crossing detector, which transduces an AC magnetic field into a square-wave magneto-optical signal. These results pave the way for axion insulators in next-generation spintronic devices.

ACKNOWLEDGMENTS

This work is supported by the National Key Research and Development Program of China (Grants No. 2024YFA1409100 and No. 2021YFA1400400), the National Natural Science Foundation of China (Grants No. 12534007, No. 92365203, and No. 12504197), the Natural Science Foundation of Jiangsu Province (Grants No. BK20253012, No. BK20252117, No. BK20243011, and No. BK20233001), the Fundamental Research Funds for the Central Universities (Grants No. KG202501 and No. 23CX06063A), the Fundamental and Interdisciplinary Disciplines Breakthrough Plan of the Ministry of Education of China (Grant No. JYB2025XDXM409), the e-Science Center of Collaborative Innovation Center of Advanced Microstructures, the Shandong Provincial Natural Science Foundation (Grant No. ZR2024QA095), and the Youth Innovation Team Plan Project for the Higher Education Institution of Shandong Province (Grant No. 2024KJN021).

DATA AVAILABILITY

The data that support the findings of this article are not publicly available. The data are available from the authors upon reasonable request.

APPENDIX A: THE EXPRESSION OF THE AVERAGE MAGNETIC ENERGY

In the macrospin approximation, the Hamiltonian can be written as

$$H = -\mathbf{B}\cdot(\mathbf{M}_A + \mathbf{M}_B) + \frac{2J}{Ng^2\mu_B^2}\mathbf{M}_A\cdot\mathbf{M}_B - \frac{D_z}{Ng^2\mu_B^2}\left[\left(M_A^z\right)^2 + \left(M_B^z\right)^2\right] \tag{A1}$$

with $\mathbf{M}_{A,B} = g\mu_B\sum_{i\in A,B}\mathbf{S}_i \approx Ng\mu_B\mathbf{S}_{A,B}$. After introducing two variables, θ_A and θ_B, which describe the angle between the magnetic moment direction and the z direction, $\mathbf{M}_{A,B}$ can be parametrized as $\mathbf{M}_{A,B} \approx M(\sin\theta_{A,B}\hat{x} + \cos\theta_{A,B}\hat{z})$, with $M = g\mu_B NS$. Now, we can get the average magnetic energy of

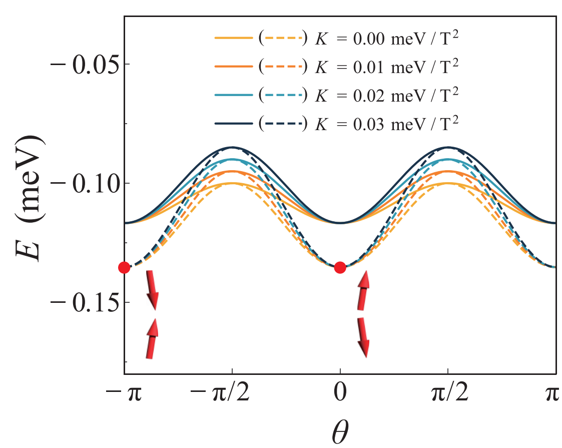

FIG. 5. Magnetic energy, including both the linear and the higher-order coupling between the Néel vector and the magnetic field, plotted as a function of the Néel vector orientation θ for different values of the higher-order coupling strength K at fixed $B_x = 0.5$ T: without (solid lines) and with (dashed lines) out-of-plane uniaxial anisotropy.

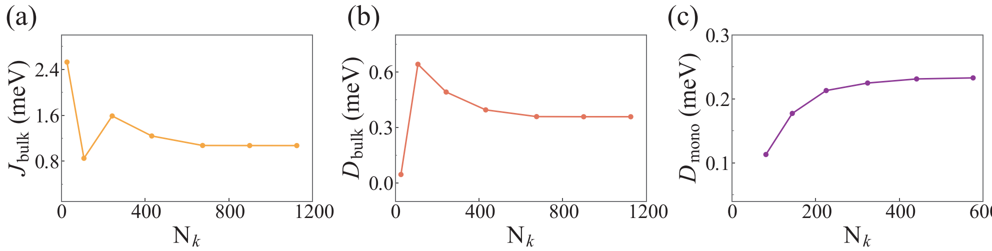

FIG. 6. The AFM exchange constant of bulk $MnBi_2Te_4$ (a) and the uniaxial magnetic anisotropy constants of bulk (b) and monolayer (c) $MnBi_2Te_4$ as functions of the number of k points.

the spin-chain model:

$$E(\theta_A, \theta_B) \equiv E_m(\theta_A, \theta_B)/NS = -g\mu_B B_x(\sin\theta_A + \sin\theta_B) - g\mu_B B_z(\cos\theta_A + \cos\theta_B) + 2JS\cos(\theta_A - \theta_B) - D_z S(\cos^2\theta_A + \cos^2\theta_B). \tag{A2}$$

We can further introduce the tilting angle, $\theta = (\theta_A + \theta_B - \pi)/2$, and the canting angle between the two sublattice spins, $\theta_c = (\theta_A - \theta_B)/2$. Then the average magnetic energy $E(\theta, \theta_c)$ can be derived as

$$E(\theta, \theta_c) = -D_z S + S\cos(2\theta_c)[2J + D_z\cos(2\theta)] + 2g\mu_B\cos\theta_c(-B_x\cos\theta + B_z\sin\theta). \tag{A3}$$

APPENDIX B: THE SYMMETRY-ALLOWED BIQUADRATIC HIGHER-ORDER COUPLING BETWEEN THE MAGNETIC FIELD AND THE NÉEL VECTOR

In addition to the linear Zeeman term, there exists a higher-order term that can further enhance the magnetic anisotropy perpendicular to the field direction. This is a biquadratic term proportional to the square of the dot product between the external magnetic field and the Néel vector:

$$H_K = \frac{KN}{(g\mu_B)^2}(\mathbf{B}\cdot\mathbf{L})^2, \tag{B1}$$

where $\mathbf{B}$ is the external magnetic field and $\mathbf{L}$ is the Néel vector, defined as $\mathbf{L} = g\mu_B(\sum_{i\in A}\mathbf{S}_i - \sum_{i\in B}\mathbf{S}_i)/N$ with A and B labeling the two AFM sublattices. We note that a similar formulation is discussed in Ref. [52].

Adopting the same approximations and parameter conventions employed in Appendix A, the average magnetic energy incorporating this higher-order term reads

$$E(\theta, \theta_c) = -D_z S + S\cos(2\theta_c)[2J + D_z\cos(2\theta)] + 4KS\sin^2\theta_c(B_z\cos\theta + B_x\sin\theta)^2 + 2g\mu_B\cos\theta_c(-B_x\cos\theta + B_z\sin\theta). \tag{B2}$$

Following the procedure outlined in the main text, we obtain the effective energy $E(\theta)$ by minimizing the energy $E(\theta, \theta_c)$ with respect to θ_c. As shown in Fig. 5, plotting the energy curves of $E(\theta)$ with different K values reveals an increase in the energy maxima, i.e., the energy of the in-plane AFM states. This enhancement is observed both in the presence and the absence of the intrinsic out-of-plane uniaxial anisotropy. Therefore, this higher-order coupling term enhances the perpendicular magnetic anisotropy by contributing a positive energy cost for any misalignment of the Néel vector from the direction normal to the field.

APPENDIX C: METHOD FOR CALCULATING THE MAGNETOELECTRIC COUPLING COEFFICIENT

Following the methodology outlined in Ref. [48], the magnetoelectric coupling coefficient α_{zz} is determined by calculating the orbital magnetization under an external electric field applied along the z direction. The orbital magnetization M_z of a film with thickness d is given by

$$M_z = \frac{e}{\hbar d}\mathrm{Im}\sum_n \int_{\varepsilon_{n\mathbf{k}}\leqslant\mu} \frac{\mathrm{d}k_x\mathrm{d}k_y}{(2\pi)^2} \times \langle\partial_{k_x}u_{n\mathbf{k}}|H_{\mathbf{k}} + \varepsilon_{n\mathbf{k}} - 2\mu|\partial_{k_y}u_{n\mathbf{k}}\rangle, \tag{C1}$$

where e is the electron charge and $\hbar$ is the reduced Plank constant. The coefficient α_{zz} is then extracted from the linear relationship:

$$M_z = \alpha_{zz}E_z, \tag{C2}$$

where E_z is the applied electric field along the z direction.

APPENDIX D: THE AFM EXCHANGE CONSTANT AND UNIAXIAL MAGNETIC ANISOTROPY CONSTANT OF $MnBi_2Te_4$

We calculate the AFM exchange constant for the bulk (J_{bulk}) and the out-of-plane uniaxial magnetic anisotropy constants for both the bulk (D_{bulk}) and the monolayer (D_{mono}) systems using different k-point meshes. As illustrated in Fig. 6, these parameters systematically converge with an increasing number of k points. The well-converged values are

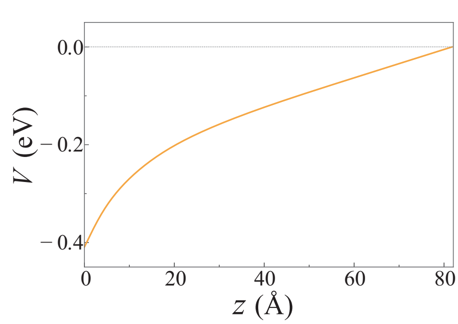

FIG. 7. The electric potential distribution along the out-of-plane direction by solving the one-dimensional Poisson equation. The zero potential point is set as the top surface of the six-SL $MnBi_2Te_4$.

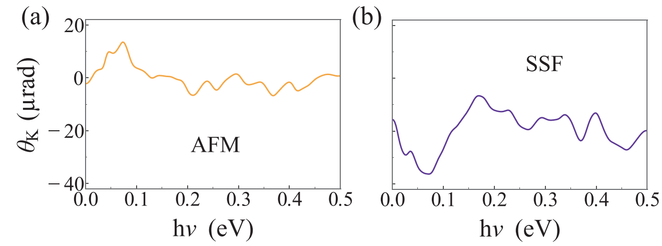

FIG. 8. Frequency-dependent Kerr rotation angles of six-SL $MnBi_2Te_4$ in the AFM state (a) and the SSF state (b).

determined to be $J_{\text{bulk}} = 1.01$ meV, $D_{\text{bulk}} = 0.35$ meV, and $D_{\text{mono}} = 0.23$ meV. We adopt these converged parameters, specifically J_{bulk} and D_{mono}, for the subsequent atomistic spin simulations of $MnBi_2Te_4$.

APPENDIX E: THE CALCULATION OF THE ELECTRIC POTENTIAL

The system's response to an external electric field is modeled by a layer-dependent electrostatic potential term, expressed as

$$H_V = \sum_{\mathbf{k}} \sum_{i,j=1}^{N} V_i \delta_{ij} c^{\dagger}_{\mathbf{k}i} c_{\mathbf{k}j}, \tag{E1}$$

where V_i is a 2×2 diagonal matrix representing the layer-resolved electrostatic potential in the top-bottom surface subspace, defined as

$$V_i = \begin{pmatrix} V_i^{\text{t}} & 0 \\ 0 & V_i^{\text{b}} \end{pmatrix}. \tag{E2}$$

Here, V_i^t and V_i^b denote the potentials at the top and bottom surfaces of the ith SL, respectively. To determine the spatial potential profile, the density of states (DOS) for the six-SL $MnBi_2Te_4$ is first extracted from first-principles calculations. Subsequently, the discretized Poisson equation is solved self-consistently in the presence of the applied electric field using the DOS. The resulting spatial profile of the potential is shown in Fig. 7.

APPENDIX F: FREQUENCY-DEPENDENT KERR ROTATION ANGLES

Based on the Dirac-fermion model and layer-resolved electric potential, the optical conductivity of the six-SL $MnBi_2Te_4$ system is calculated using the Kubo-Greenwood formalism. Subsequently, the frequency-dependent Kerr rotation angles are calculated for both the AFM and the SSF states, following the method described in Ref. [53]. The resulting Kerr rotations are presented in Fig. 8.

APPENDIX G: ATOMISTIC SPIN SIMULATIONS OF THE TWO-SPIN SYSTEM

To verify our theoretical analysis from dynamics, we have performed atomistic spin simulations for a two-spin system based on the Landau-Lifshitz-Gilbert equation, as shown in Fig. 9. The simulation results agree well with our model analysis: if the external field is along the in-plane direction, the

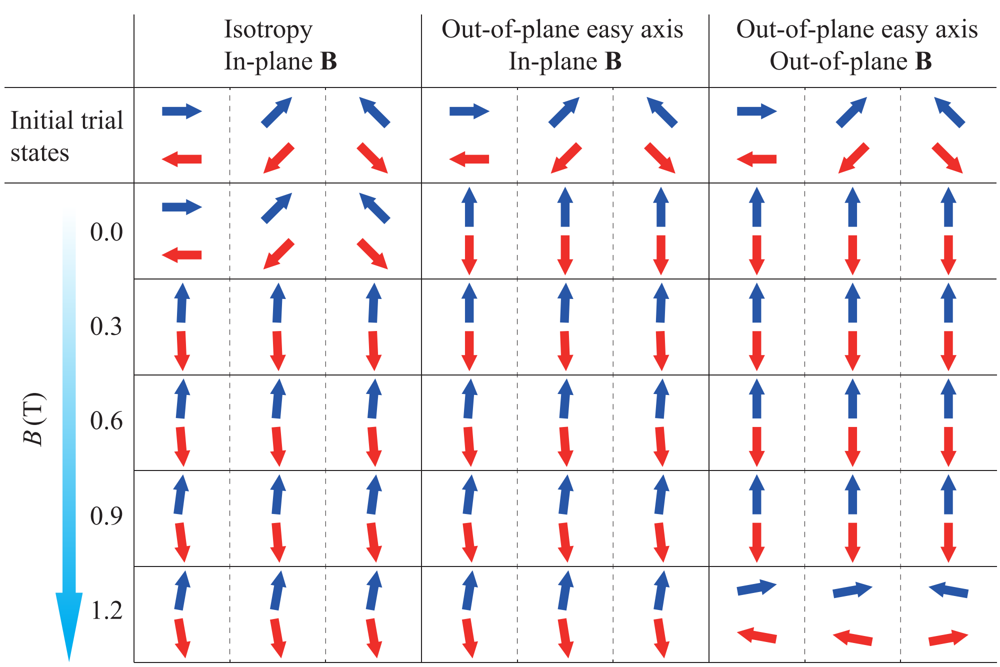

FIG. 9. Atomistic spin simulations of the two-spin system in different initial trial states and values of field, containing three different anisotropies and magnetic field configurations: Isotropy with in-plane field, Out-of-plane easy axis with in-plane field, and Out-of-plane easy axis with out-of-plane field.

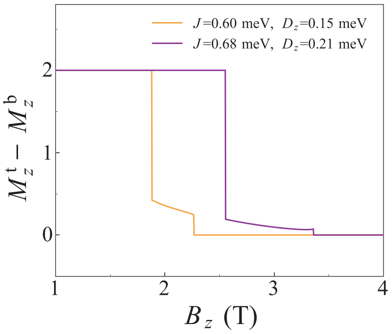

FIG. 10. Simulated difference between the z components of the normalized magnetic moments for the top and bottom surfaces as a function of the out-of-plane magnetic field B_z. The yellow curve ($J = 0.60$ meV, $D_z = 0.15$ meV) and the purple curve ($J = 0.68$ meV, $D_z = 0.21$ meV) demonstrate SSF transitions at 1.88 and 2.55 T, respectively. The magnetic moment is taken as $M_s = 5\mu_B$.

AFM order favors the out-of-plane direction; if the external field is along the out-of-plane direction and there is an out-of-plane easy axis, when the field is large enough, there will be a spin-flop transition, during which the AFM order reorients from the out-of-plane to the in-plane direction, with a slight tilt toward the field direction.

APPENDIX H: REFINEMENT OF THE SSF TRANSITION FIELD BASED ON EXPERIMENTS

While the atomistic spin simulation based on the first-principles parameters in the main text successfully exhibits the SSF transition, the experimental transition field in $MnBi_2Te_4$ is known to be highly sample dependent [27,32,39]. To illustrate how specific experimental results can inform and refine our theoretical model, we perform additional simulations by adjusting the magnetic parameters.

As shown in Fig. 10, tuning the AFM exchange constant J and the magnetic anisotropy constant D_z allows us to reproduce different experimental results quantitatively. For instance, $J = 0.60$ meV and $D_z = 0.15$ meV yield an SSF transition field of 1.88 T, well within the 1–2 T range recently reported in Ref. [32]. Furthermore, the experimentally extracted parameters from Ref. [39] ($J = 0.68$ meV and $D_z = 0.21$ meV) result in a simulated transition field of 2.55 T, consistent with their direct observations. These results demonstrate that our model can reproduce the different transition fields reported in experiments. Although the transition field varies with the choice of parameters, the overall features of the SSF transition remain essentially unchanged, indicating that our model captures the essential physics of the transition.

[1] R. Li, J. Wang, X. L. Qi, and S. C. Zhang, Dynamical axion field in topological magnetic insulators, Nat. Phys. **6**, 284 (2010).
[2] X. L. Qi and S. C. Zhang, Topological insulators and superconductors, Rev. Mod. Phys. **83**, 1057 (2011).
[3] F. Wilczek, Two applications of axion electrodynamics, Phys. Rev. Lett. **58**, 1799 (1987).
[4] A. M. Essin, J. E. Moore, and D. Vanderbilt, Magnetoelectric polarizability and axion electrodynamics in crystalline insulators, Phys. Rev. Lett. **102**, 146805 (2009).
[5] D. M. Nenno, C. A. C. Garcia, J. Gooth, C. Felser, and P. Narang, Axion physics in condensed-matter systems, Nat. Rev. Phys. **2**, 682 (2020).
[6] A. Sekine and K. Nomura, Axion electrodynamics in topological materials, J. Appl. Phys. **129**, 141101 (2021).
[7] L. Wu, M. Salehi, N. Koirala, J. Moon, S. Oh, and N. P. Armitage, Quantized Faraday and Kerr rotation and axion electrodynamics of a 3D topological insulator, Science **354**, 1124 (2016).
[8] K. N. Okada, Y. Takahashi, M. Mogi, R. Yoshimi, A. Tsukazaki, K. S. Takahashi, N. Ogawa, M. Kawasaki, and Y. Tokura, Terahertz spectroscopy on Faraday and Kerr rotations in a quantum anomalous Hall state, Nat. Commun. **7**, 12245 (2016).
[9] M. Mogi, Y. Okamura, M. Kawamura, R. Yoshimi, K. Yasuda, A. Tsukazaki, K. S. Takahashi, T. Morimoto, N. Nagaosa, M. Kawasaki, Y. Takahashi, and Y. Tokura, Experimental signature of the parity anomaly in a semi-magnetic topological insulator, Nat. Phys. **18**, 390 (2022).
[10] M. Gu, J. Li, H. Sun, Y. Zhao, C. Liu, J. Liu, H. Lu, and Q. Liu, Spectral signatures of the surface anomalous Hall effect in magnetic axion insulators, Nat. Commun. **12**, 3524 (2021).
[11] M. Gong, H. Liu, H. Jiang, C. Z. Chen, and X. C. Xie, Half-quantized helical hinge currents in axion insulators, Natl. Sci. Rev. **10**, nwad025 (2023).
[12] Y. Feng, X. Feng, Y. Ou, J. Wang, C. Liu, L. Zhang, D. Zhao, G. Jiang, S. C. Zhang, K. He, X. Ma, Q. K. Xue, and Y. Wang, Observation of the zero Hall plateau in a quantum anomalous Hall insulator, Phys. Rev. Lett. **115**, 126801 (2015).
[13] M. Mogi, M. Kawamura, R. Yoshimi, A. Tsukazaki, Y. Kozuka, N. Shirakawa, K. Takahashi, M. Kawasaki, and Y. Tokura, A magnetic heterostructure of topological insulators as a candidate for an axion insulator, Nat. Mater. **16**, 516 (2017).
[14] D. Xiao, J. Jiang, J. H. Shin, W. Wang, F. Wang, Y. F. Zhao, C. Liu, W. Wu, Moses H. W. Chan, N. Samarth, and C. Z. Chang, Realization of the axion insulator state in quantum anomalous Hall sandwich heterostructures, Phys. Rev. Lett. **120**, 056801 (2018).
[15] Y. Tokura, K. Yasuda, and A. Tsukazaki, Magnetic topological insulators, Nat. Rev. Phys. **1**, 126 (2019).
[16] C. Liu, Y. Wang, H. Li, Y. Wu, Y. Li, J. Li, K. He, Y. Xu, J. Zhang, and Y. Wang, Robust axion insulator and Chern insulator phases in a two-dimensional antiferromagnetic topological insulator, Nat. Mater. **19**, 522 (2020).
[17] M. M. Otrokov *et al.*, Prediction and observation of an antiferromagnetic topological insulator, Nature (London) **576**, 416 (2019).
[18] Y. Gong *et al.*, Experimental realization of an intrinsic magnetic topological insulator, Chin. Phys. Lett. **36**, 076801 (2019).
[19] J. Li, Y. Li, S. Du, Z. Wang, B. L. Gu, S. C. Zhang, K. He, W. Duan, and Y. Xu, Intrinsic magnetic topological insulators in van der Waals layered $MnBi_2Te_4$-family materials, Sci. Adv. **5**, eaaw5685 (2019).
[20] D. Zhang, M. Shi, T. Zhu, D. Xing, H. Zhang, and J. Wang, Topological axion states in the magnetic insulator $MnBi_2Te_4$ with the quantized magnetoelectric effect, Phys. Rev. Lett. **122**, 206401 (2019).

[21] B. Chen *et al.*, Intrinsic magnetic topological insulator phases in the Sb doped $MnBi_2Te_4$ bulks and thin flakes, Nat. Commun. **10**, 4469 (2019).

[22] Y. J. Chen, L. X. Xu, J. H. Li, Y. W. Li, H. Y. Wang, C. F. Zhang, H. Li, Y. Wu, A. J. Liang, C. Chen, S. W. Jung, C. Cacho, Y. H. Mao, S. Liu, M. X. Wang, Y. F. Guo, Y. Xu, Z. K. Liu, L. X. Yang, and Y. L. Chen, Topological electronic structure and its temperature evolution in antiferromagnetic topological insulator $MnBi_2Te_4$, Phys. Rev. X **9**, 041040 (2019).

[23] Y. J. Hao *et al.*, Gapless surface Dirac cone in antiferromagnetic topological insulator $MnBi_2Te_4$, Phys. Rev. X **9**, 041038 (2019).

[24] H. Li *et al.*, Dirac surface states in intrinsic magnetic topological insulators $EuSn_2As_2$ and $MnBi_{2n}Te_{3n+1}$, Phys. Rev. X **9**, 041039 (2019).

[25] Y. Deng, Y. Yu, M. Z. Shi, Z. Guo, Z. Xu, J. Wang, X. H. Chen, and Y. Zhang, Quantum anomalous Hall effect in intrinsic magnetic topological insulator $MnBi_2Te_4$, Science **367**, 895 (2020).

[26] J. Ge, Y. Liu, J. Li, H. Li, T. Luo, Y. Wu, Y. Xu, and J. Wang, High-Chern-number and high-temperature quantum Hall effect without Landau levels, Natl. Sci. Rev. **7**, 1280 (2020).

[27] Z. Lian, Y. Wang, Y. Wang, W. H. Dong, Y. Feng, Z. Dong, M. Ma, S. Yang, L. Xu, Y. Li, B. Fu, Y. Li, W. Jiang, Y. Xu, C. Liu, J. Zhang, and Y. Wang, Antiferromagnetic quantum anomalous Hall effect under spin flips and flops, Nature (London) **641**, 70 (2025).

[28] Y. Wang, B. Fu, Y. Wang, Z. Lian, S. Yang, Y. Li, L. Xu, Z. Gao, X. Yang, W. Wang, W. Jiang, J. Zhang, Y. Wang, and C. Liu, Towards the quantized anomalous Hall effect in AlO_x-capped $MnBi_2Te_4$, Nat. Commun. **16**, 1727 (2025).

[29] C. Zhang, X. Lu, N. Wang, T. Huang, H. Zhang, N. Cao, A. Wang, X. Zhou, K. Watanabe, T. Taniguchi, S. Y. Xu, and W. Gao, Zero-field chiral edge transport in an intrinsic magnetic topological insulator $MnBi_2Te_4$, Nat. Commun. **16**, 5587 (2025).

[30] T. Zhu, H. Wang, H. Zhang, and D. Xing, Tunable dynamical magnetoelectric effect in antiferromagnetic topological insulator $MnBi_2Te_4$ films, npj Comput. Mater. **7**, 121 (2021).

[31] A. Gao *et al.*, Layer Hall effect in a 2D topological axion antiferromagnet, Nature (London) **595**, 521 (2021).

[32] J. X. Qiu *et al.*, Observation of the axion quasiparticle in 2D $MnBi_2Te_4$, Nature (London) **641**, 62 (2025).

[33] N. Wang, D. Kaplan, Z. Zhang, T. Holder, N. Cao, A. Wang, X. Zhou, F. Zhou, Z. Jiang, C. Zhang, S. Ru, H. Cai, K. Watanabe, T. Taniguchi, B. Yan, and W. Gao, Quantum-metric-induced nonlinear transport in a topological antiferromagnet, Nature (London) **621**, 487 (2023).

[34] A. Gao *et al.*, Quantum metric nonlinear Hall effect in a topological antiferromagnetic heterostructure, Science **381**, 181 (2023).

[35] Y. Xiao, H. Wang, D. Wang, R. Lu, X. Yan, H. Guo, C. M. Hu, K. Xia, H. Zhang, and D. Xing, Nonlinear level attraction of cavity axion polariton in antiferromagnetic topological insulator, Phys. Rev. B **104**, 115147 (2021).

[36] T. Zhu, H. Wang, D. Xing, and H. Zhang, Axionic surface wave in dynamical axion insulators, Phys. Rev. B **106**, 075103 (2022).

[37] P. M. Sass, J. Kim, D. Vanderbilt, J. Yan, and W. Wu, Robust *A*-type order and spin-flop transition on the surface of the antiferromagnetic topological insulator $MnBi_2Te_4$, Phys. Rev. Lett. **125**, 037201 (2020).

[38] B. Li, J. Q. Yan, D. M. Pajerowski, E. Gordon, A. M. Nedić, Y. Sizyuk, L. Ke, P. P. Orth, D. Vaknin, and R. J. McQueeney, Competing magnetic interactions in the antiferromagnetic topological insulator $MnBi_2Te_4$, Phys. Rev. Lett. **124**, 167204 (2020).

[39] S. Yang, X. Xu, Y. Zhu, R. Niu, C. Xu, Y. Peng, X. Cheng, X. Jia, Y. Huang, X. Xu, J. Lu, and Y. Ye, Odd-even layer-number effect and layer-dependent magnetic phase diagrams in $MnBi_2Te_4$, Phys. Rev. X **11**, 011003 (2021).

[40] X. Yang, Y. Wang, C. Lu, Y. Wang, Z. Lian, Z. Liu, Y. Chen, J. Zhang, Y. Wang, C. Liu, and W. Wang, Tailoring Néel orders in layered topological antiferromagnet $MnBi_2Te_4$, Phys. Rev. Lett. **135**, 266704 (2025).

[41] H. Wang and H. Zhang, Cascade quantum transitions in antiferromagnetic quantum anomalous Hall effect, Sci. China: Phys. Mech. Astron. **68**, 297031 (2025).

[42] G. Kresse and D. Joubert, From ultrasoft pseudopotentials to the projector augmented-wave method, Phys. Rev. B **59**, 1758 (1999).

[43] G. Kresse and J. Furthmüller, Efficient iterative schemes for *ab initio* total-energy calculations using a plane-wave basis set, Phys. Rev. B **54**, 11169 (1996).

[44] H. Wang, D. Wang, Z. Yang, M. Shi, J. Ruan, D. Xing, J. Wang, and H. Zhang, Dynamical axion state with hidden pseudospin Chern numbers in $MnBi_2Te_4$-based heterostructures, Phys. Rev. B **101**, 081109(R) (2020).

[45] Z. Liu and J. Wang, Anisotropic topological magnetoelectric effect in axion insulators, Phys. Rev. B **101**, 205130 (2020).

[46] C. Lei, S. Chen, and A. H. MacDonald, Magnetized topological insulator multilayers, Proc. Natl. Acad. Sci. USA **117**, 27224 (2020).

[47] D. Wang, H. Wang, and H. Zhang, Dirac fermion approach and its application to design high Chern numbers in magnetic topological insulator multilayers, Phys. Rev. B **107**, 155114 (2023).

[48] R. Mei, Y. F. Zhao, C. Wang, Y. Ren, D. Xiao, C. Z. Chang, and C. X. Liu, Electrically controlled anomalous Hall effect and orbital magnetization in topological magnet $MnBi_2Te_4$, Phys. Rev. Lett. **132**, 066604 (2024).

[49] Y. Fan, H. Wang, P. Tang, S. Murakami, X. Wan, H. Zhang, and D. Xing, Symmetry-driven anisotropic coupling effect in antiferromagnetic topological insulator: Mechanism for a quantum anomalous Hall state with a high Chern number, Phys. Rev. B **110**, 035139 (2024).

[50] P. Kollar, J. Fuzer, R. Bures, and M. Faberova, AC magnetic properties of Fe-based composite materials, IEEE Trans. Magn. **46**, 467 (2010).

[51] J. Zak, E. R. Moog, C. Liu, and S. D. Bader, Magneto-optics of multilayers with arbitrary magnetization directions, Phys. Rev. B **43**, 6423 (1991).

[52] D. I. Khomskii, *Basic Aspects of the Quantum Theory of Solids: Order and Elementary Excitations* (Cambridge University Press, Cambridge, 2010).

[53] W. Feng, J. P. Hanke, X. Zhou, G. Y. Guo, S. Blügel, Y. Mokrousov, and Y. Yao, Topological magneto-optical effects and their quantization in noncoplanar antiferromagnets, Nat. Commun. **11**, 118 (2020).